HAL
archives-ouvertes.fr

Effect of nitrogen on the amorphous structure and subthreshold electrical conduction of GeSeSb-based OTS thin films

Anthonin Verdy, Francesco d'Acapito, Jean-Baptiste Dory, Gabriele Navarro, Mathieu Bernard, Pierre Noé

▶ To cite this version:

Anthonin Verdy, Francesco d'Acapito, Jean-Baptiste Dory, Gabriele Navarro, Mathieu Bernard, et al.. Effect of nitrogen on the amorphous structure and subthreshold electrical conduction of GeSeSb-based OTS thin films. physica status solidi (RRL) - Rapid Research Letters, Wiley-VCH Verlag, In press. cea-02865466

HAL Id: cea-02865466
https://hal-cea.archives-ouvertes.fr/cea-02865466

Submitted on 11 Jun 2020

HAL is a multi-disciplinary open access archive for the deposit and dissemination of scientific research documents, whether they are published or not. The documents may come from teaching and research institutions in France or abroad, or from public or private research centers.

L'archive ouverte pluridisciplinaire HAL, est destinée au dépôt et à la diffusion de documents scientifiques de niveau recherche, publiés ou non, émanant des établissements d'enseignement et de recherche français ou étrangers, des laboratoires publics ou privés.

Effect of nitrogen on the amorphous structure and subthreshold electrical conduction of GeSeSb-based OTS thin films

Anthonin Verdy, Francesco d'Acapito, Jean-Baptiste Dory, Gabriele Navarro*, Mathieu Bernard, and Pierre Noé**

A. Verdy, J.-B Dory, Dr. G. Navarro, Dr. M. Bernard, Dr. P. Noé
CEA-LETI, Univ. Grenoble Alpes, F-38000 Grenoble, France.
E-mail: anthonin.verdy@cea.fr, pierre.noe@cea.fr & gabriele.navarro@cea.fr

Dr. F. d'Acapito
CNR-IOM-OGG c/o ESRF – The European Synchrotron, 71 rue des Martyrs, F-38043 Grenoble, France.

Keywords: chalcogenide, OTS, memory, XAS, EXAFS, Ge, Se, Sb, N

Abstract

In this study, the amorphous structure of Ge-Se-Sb-N chalcogenide thin films is investigated through Raman, Infrared and X-ray Absorption Spectroscopies in the light of the electrical performances of such materials once integrated in OTS selector devices. In particular, we show that the presence of homopolar and wrong bonds in the amorphous structure has a detrimental impact on the subthreshold leakage current of OTS devices. Whereas the presence of Sb-Sb and Ge-Sb bonds tends to increase the leakage current in pristine devices, the presence of Se-Se bonds is correlated to a significant device-to-device dispersion of sub-threshold characteristics after the device initialization. Finally, the incorporation of a proper N concentration in Ge-Se-Sb glass permits to suppress the homopolar bonds, leading to a very low leakage current and a low device-to-device dispersion.

1. Introduction

Resistive crossbar arrays represent nowadays a valuable solution for the design of innovative memory systems for Storage Class Memory applications. In this architecture, the memory element is located at the intersection of the word-lines and the bit-lines.[1] Such parallelism induces the inherent creation of sneak paths and leakage currents (I_{leak}) that can induce cell-to-cell disturbances upon programming, as well as cell reading fails. Therefore, each resistive memory cell (1R) of the crossbar array requires to be integrated in the Back-end-Of-Line (BEOL) in series with a BEOL selector (1S) to form a so-called 1S1R device. The BEOL selector device has the function to replace the commonly used selection made by a transistor. Among the different BEOL selectors technologies that are studied in the literature, the one based on Ovonic Threshold Switching (OTS) materials represents one of the best and most promising technological solution, as demonstrated by the recent commercialization of the Optane memory by Intel and the intense research and developments around OTS in the last years.[2–10]

OTS materials are amorphous chalcogenide exhibiting the unique property, upon electric-field application, to switch from a highly resistive state, the OFF-state, to a metastable conductive state, the ON-state, when the applied voltage exceeds the threshold voltage V_{th}.[11] When the ON-state current is decreased below the holding current I_h, the material recovers its highly resistive OFF-state. A typical current-voltage characteristic of an OTS device is reported in **Figure 1a**. The OFF-state is responsible for the leakage current in unselected cells, whereas the ON-state is used for the programming and the reading operations of the memory device.

OTS selectors have to fill different requirements that depend also on the electrical parameters of the memory element. It should ensure an optimized threshold voltage to limit unwanted switching events, a threshold current compatible with the co-integrated resistive memory, a low leakage current I_{leak} (i.e. low OFF-state current) and a thermal stability compatible with CMOS BEOL integration for which the material could typically experience a thermal stress of about 400 °C.[12] Most of the OTS materials that fulfill all these specifications are chalcogenide glasses composed by one or more chalcogen elements,

in general Se and/or Te, glass former elements such as Ge, Si or As and sometimes light dopant elements such as N or C atoms. Thus, OTS materials are quite complex amorphous materials and the control of their structure and of their properties becomes a key challenge for applications.

In this paper, by means of the material engineering of Ge-Se-Sb-N system, we evidence the link between the local order in the amorphous structure of OTS materials, investigated by Raman, Infrared and Extended X-Ray Absorption Fine Structure spectroscopies, and the subthreshold current behavior when integrated in selector devices. Despite Sb incorporation in Ge-Se films allows to significantly decrease the threshold voltage of such glasses[13], it exhibits the major hindering drawback of decreasing the thermal stability against undesired crystallization, leading to the detrimental increase of the leakage current.[14] In that context, besides the incorporation of N in Ge-Se-Sb films permits to increase the amorphous phase stability, we evidence its beneficial impact on reducing the leakage current in $Ge_{24}Se_{56}Sb_{20}$ (GSS) film. Finally, we discuss the link between such device performances and the amorphous structure of GSS films exhibiting different N concentrations

2. Electrical results

OTS selector devices require a first initialization step called "firing". This first switching event occurs at a higher voltage value (fire voltage or V_{fire}) than the one used in all the following switching operations (threshold voltage or V_{th}). Moreover, an increase of I_{leak} is observed after the firing. **Figure 1b** shows the evolution of the leakage current measured at $V_{th}/2$ before (i.e. on as-fabricated pristine device) and after firing (i.e. after the application of the first electrical pulse) for $Ge_{24}Se_{56}Sb_{20}$ (GSS) thin films as a function of N concentration labeled as N_x, being x representative of the N_2 flow used in Ar/N_2 plasma of the reactive sputtering deposition process (see also the I-V characteristics plotted in **Figure S1** in **Supplementary Information**). The GSS film free of N exhibits a pristine leakage current of about 10^{-10} A that drastically increases of more than two orders of magnitude up to 10^{-8} A after the firing. When N is incorporated in GSS, we observe a reduction of the pristine leakage current below 10^{-}

^{11} A and an increase of only about one order of magnitude of the post-firing leakage current. However, whereas the variability of the leakage current values of pristine devices is small, with data almost distributed all around the median, N doping in GSS films seems to induce an important increase of the dispersion on the post-firing leakage currents with a large spread towards the high current values. Indeed, for high N content we observe a large spread of the data over three orders of magnitude. However, for a specific N content (N_2) in GSS film, low leakage current values with low variability are observed, even after firing. Thus, even if N doping is beneficial for the improvement of the thermal stability and the reduction of the leakage current, the N content has to be carefully dosed. In order to get a better insight on such phenomenon we performed a detailed analysis of the impact of N incorporation on the amorphous structure of GSS films.

3. Amorphous structure

To understand the role of N-doping in GSS, the amorphous structure of GSS films with different N contents was investigated using Raman, Infrared and Extended X-Ray Absorption Fine Structure (EXAFS) spectroscopies. All these complementary techniques are powerful tools to easily get information on the local structure and the bonding configuration inside the amorphous material. **Figure 2a** shows the Raman spectra measured on GSS films as a function of the N content (see the **Experimental Section**). N-free GSS film is characterized by the Raman modes of Ge-Se and Sb-Se bonds. The Ge-Se Raman modes are located at 200 and 215 cm^{-1} corresponding to Ge-Se vibration in corner- and edge-sharing $GeSe_{4/2}$ tetrahedrons, respectively.[15–18] The Raman modes of Sb-Se bonds appear at 190 cm^{-1} and correspond to Sb-Se vibrations in $SbSe_{3/2}$ pyramids.[16,19] Moreover, an intense mode around 160 cm^{-1} is also observed and can be attributed to Sb-Sb bonds in Se_2Sb-$SbSe_2$ ethane-like motifs.[16,19] When N is incorporated in GSS, this Sb-Sb mode progressively vanishes. When the N_2 composition is reached, the Sb-Sb shoulder at 160 cm^{-1} is not further visible but for higher N content, a mode near 260 cm^{-1} progressively appears and can be attributed to Se-Se vibrations.[15,17]

In **Figure 2b** are shown the FTIR spectra of the different GSS films acquired in the Ge-N absorption range (see the **Experimental Section**). Surprisingly, when N is incorporated in GSS a broad absorption band with multiple contributions located at ~650 cm^{-1} and ~750 cm^{-1} appears and progressively increases with the N content. It must be emphasized here that this double absorption peak does not perfectly match with the expected single contribution usually observed near 700 cm^{-1} for amorphous GeN_x films.[20–22] In our case, the splitting of the main FTIR absorption band can be the result of the presence of different environments around the localized Ge-Ge-N bonds and GeN_x motifs in the amorphous matrix. Indeed, *ab initio* simulations predicted that the local atomic configuration around N atoms in N-doped amorphous GeTe phase-change materials thin films consists of two structural main motifs (NGe_3 pyramids and NGe_4 tetrahedra) at the origin of two slightly separated absorption bands.[23] However, the experimental FTIR spectra of N-doped GeTe films do not exhibit such bi-modal contribution. This could be the result of the slight discrepancy generally observed in the amorphous structure between N-doped GeTe films obtained by sputtering deposition and the melt-quenched glasses of the simulations.[24] Nevertheless, the presence of different atomic environments has also been studied in N-doped $Ge_2Sb_2Te_5$ films, in which a Ge nitride phase separation occurs when nitrogen is incorporated, leading to the formation of two amorphous phases.[25] It is also demonstrated that this phase separation appears predominantly for high N-content. Such an observation is in accordance with our FTIR spectra for which the two contributions of the bimodal IR absorption peak become more and more well defined as the N content is increased.

In order to get more information on the local order in our amorphous materials, the films were analyzed by grazing incidence X-ray Absorption Spectroscopy (GIXAS) acquired at the Ge, Se and Sb K-egdes (see the **Experimental Section**). The EXAFS spectra and the corresponding Fourier Transforms of N-doped and undoped GSS layers extracted from the XAS acquisitions are plotted in **Figure 3** (see **Experimental Section** for raw data treatment procedure, details on fitting procedure for the quantitative analysis of EXAFS, and **Figure S2** and **Table S3** of the **Supplementary Information** for

quantitative results on atomic neighbors, coordination numbers and interatomic distances). As shown in **Figure 3b** and listed in **Table S3**, the EXAFS data clearly confirm the presence of Ge-Se and Sb-Se bonds at R_{Ge-Se}~2.39 Å and R_{Sb-Se}~2.64 Å in the GSS films, as well as the presence and increasing number of Ge-N bonds at R~1.84 Å after N incorporation. However, XAS analysis also reveals the presence of Ge-Sb bonds at R_{Ge-Sb}~2.64 Å in the GSS film, not visible in Raman and IR characterizations, as well as the possible formation of Sb-N bonds at R_{Sb-N}~2 Å when N is incorporated in the GSS matrix. These results are in good agreement with previous EXAFS, Neutron Diffraction and X-Ray Diffraction study on Ge-Se-Sb materials.[26] From the point of view of coordination numbers, quantitative EXAFS analyses follow approximately the so-called Mott rule generally used as reference in such systems[27]. The slight deviations could be ascribed to the limit of the accuracy of the Mott rule (that predicts the total coordination number of an element as 8-N, N being the number of s and p electrons in the valence shell of the considered element) as well as to the unavoidable noise in the fluorescence collected data and correlations between amplitude parameters (N and σ). Note that in XAS it is not possible to distinguish X-Se from X-Ge scattering paths, the electronic density of Ge and Se atoms being to close. Thus, the considered environments are Se-(Ge/Se) and Sb-(Ge/Se). EXAFS measurements confirms the presence of Sb-Sb bonds as well as Sb-(Ge/Se) bonds.

4. Discussion

Due to a more favorable enthalpy of formation, Se atoms are preferentially linked to Ge atoms than to Sb atoms in GSS.[28] Our GSS films ($Ge_{24}Se_{56}Sb_{20}$) are chalcogen-deficient compared to $GeSe_2$ and Sb_2Se_3 stoichiometric compositions and to compounds lying on the $GeSe_2$-Sb_2Se_3 pseudo-binary tie-line. As a result, in our Se-deficient and Sb-rich GSS films, Sb-Sb bonds are thus promoted and appear in ethane-like Se_2Sb-$SbSe_2$ motifs as observed in Raman spectra at 160 cm^{-1}. Moreover, the absence of shoulder or peak in Raman spectra near 140 cm^{-1} corresponding to the main Raman mode of amorphous a-Sb phase[29] indicates that there is no segregation or formation of a-Sb phase or

Sb-clusters in GSS film. However, since Raman modes of Ge-Se and Sb-Se expected respectively at 200 and 190 cm^{-1} are very close, it is difficult to confirm the presence of Sb-Se bonds only on the basis of the Raman spectra. EXAFS measurements permit to confirm unambiguously the presence of Sb-Se bonds as well as Sb-Sb bonds in GSS film. Moreover, EXAFS quantitative analysis gives a Sb-Sb coordination number $CN_{Sb-Sb} = 0.8 \pm 0.3$ that is close to 1, confirming its most probable presence in ethane-like Se_2Sb-$SbSe_2$ motifs as observed on Raman spectra rather than in a nano-segregated Sb phase for which significantly higher CN_{Sb-Sb} would be expected.[30] Despite the lower CN of Sb-Sb bonds compared to Ge-Se ones, the intensity of the Sb-Sb Raman mode at 160 cm^{-1} is surprisingly close to the one of Ge-Se modes. This effect could be the result of the higher polarizability of Sb bonds,[31] meaning that the relative intensity is not relevant to quantify the bonds proportion. EXAFS analysis also reveals that the excess of Sb tends to create wrong Ge-Sb bonds that are less probable but previously observed when Sb is incorporated in excess in Ge-Sb-Se glasses.[26] Wrong (Ge-Sb) and homopolar (Sb-Sb) bond are known to significantly affect the electronic density of states (DoS) of amorphous chalcogenide with introduction of band tail and mid-gap states.[32–35] These defect states have been held responsible for an increase of the subthreshold current I_{leak} due to an increase of the Poole-Frenkel transport.[36–38] The increased density of the electronic defect states and the reduction of the energy barrier for the electrons promote the charge hopping and therefore an increase of the electrical conductivity of the OTS material. Moreover, Sb is known to deteriorate the thermal stability of Ge-Se compositions, promoting the segregation and crystallization of Se and Sb-Se phases.[14,39] These local segregation can be at the origin of the significant increase by several orders of magnitude of the leakage current after the firing, as shown in **Figure 1b**, and resulting from the important Joule heating that can be expected when the current flow through the device in the ON-state.

The reduction of the number of homopolar Sb-Sb bonds can be achieved by decreasing the Ge content (i.e. increasing the Se concentration), in order to increase the fraction of Se bonded to Sb. However, Ge being a good glass former in chalcogenide glasses, decreasing the Ge concentration is not

suitable for OTS applications since it can lead to a detrimental degradation of the thermal stability of the material. Thus, for this purpose N-doping is preferable. Indeed, upon increasing the N concentration in GSS films, a progressive formation of Ge-N bonds occurs at the expense of the Ge-Se bonds, as depicted by the decrease of Ge-(Se+Sb) CN. More and more Se atoms are released and available to form bonds with Sb. This is evidenced in Raman spectra, where the Sb-Sb mode progressively vanishes as the N content in GSS films is increased, as well as in FTIR spectra where the Ge-N absorption band concurrently increases. The same trend is also seen in the EXAFS analysis where all Ge-N, Sb-(Se/Ge) and Se-Sb CNs increase with the N concentration. For the highest N contents, being the valence of Sb atoms fully filled, Se-Se bonds progressively appears in the Raman spectra at 260 cm^{-1}.

From all above observations, the most interesting feature is that for a specific N content (sample GSS-N_2), no homopolar Sb-Sb nor Se-Se bonds are detected in the amorphous by both Raman and EXAFS spectroscopies. The reduction of detrimental Sb-Sb and Ge-Sb electronic defect bonds thanks to N-doping leads to a decrease of the pristine leakage current below 10^{-11} A for N-doped GSS samples, which represents a reduction of more than one order of magnitude compared to un-doped GSS. Moreover, after firing, an increase of the leakage current of only about one order of magnitude is observed. We think that beyond the removal of homopolar and wrong bonds, N-doping also increases the glass rigidity and amorphous phase stability thanks to the formation of strong Ge-N and Sb-N covalent bonds. Indeed, it was demonstrated that an optimized N-doped GSS OTS material called GSSN (corresponding to the sample here labeled as GSS-N_2) is able to sustain high temperature annealing of 400 °C while keeping state-of-the-art OTS performances.[38]

For upper N concentrations (N_2 flow > N_2), the formation of Se-Se bonds observed in the Raman spectra does not induce any significant increase of the pristine leakage current measured before the firing, probably thanks to the high band gap of amorphous selenium of 1.9-2 eV.[40] But after the firing, such devices exhibit the highest dispersion in leakage current values spreading over two up to three decades (**Figure 1b**). On the contrary, GSS-N_2, for which there is no evidence of the presence of

Se-Se bonds, shows the smallest dispersion of leakage currents, even after the firing. We think that the increase of the dispersion in the samples with high N concentration can be the result of the stochastic formation of localized conductive paths during the firing step. This can result from the decrease of the amorphous phase stability induced by Sb incorporation, but also from the local formation of metallic Se[41] clusters or chains in the films. Indeed, the thermal stress induced by the Joule heating effect, occurring when the current flows through the device in the ON state, can boost such phenomenon. Such localized segregation and crystallization in the OTS films can increase randomly the leakage current of the devices after the firing.

The main structural features as a function of the N content in GSS OTS films are summarized in **Figure 4** with a plot of the relative change in number Sb-Sb, Ge-N and Se-Se bond derived from the integral of corresponding Raman and IR modes. The number of homopolar and wrong bonds reaches its minimum and becomes equal to zero for the optimized GSS-N_2 sample that exhibits the best performance in terms of leakage current values and current dispersion.

5. Conclusions

We studied the link between bonding configurations in amorphous structure of N-doped Ge-Se-Sb chalcogenide thin films and their performances when incorporated in OTS selector devices. A particular emphasis was made on their subthreshold current characteristics currents that are shown to be dependent on the material composition. We demonstrated that the presence of homopolar/wrong bonds in the amorphous OTS materials, mostly Ge-Sb, Sb-Sb and Se-Se bonds, is detrimental for OTS reliability. In particular, homopolar/wrong bonds such as Sb-Sb or Ge-Sb induce an increase of the leakage current of the pristine OTS devices that is worsened further after the initial firing step. The formation of Se-Se homopolar bonds resulting from a too high N concentration in Ge-Se-Sb-N films has no significant impact on the leakage current of as-fabricated pristine OTS devices but induces a highly dispersed leakage current values after the firing operation. Finally, we demonstrate that the

introduction of N in Ge-Se-Sb films is fundamental in order to avoid undesired bonds. Adjusting the N concentration in order to form Ge-N and Sb-N bonds permits to remove Sb-Sb and Ge-Sb bonds, responsible for the increase of the leakage current. Nevertheless, for highest N contents, the formation of a high concentration of Ge-N bonds (and in a less extent Sb-N bonds) tends to release Se atoms that can form Se-Se homopolars, leading to the Se segregation that is detrimental for the post-firing OTS leakage current variability. Hence, the optimization of the N concentration in Ge-Se-Sb films allows to drastically limit the presence of homopolar/wrong bonds and enables state-of-the-art OTS devices with very low leakage current, high thermal stability and lowest device-to-device variability of sub-threshold characteristics.

6. Experimental section

OTS thin films were deposited in an industrial magnetron sputtering cluster tool on 200 mm Si-based substrates by magnetron co-sputtering from high purity $Ge_{30}Se_{70}$ and Sb targets. The introduction of N in the Ge-Se-Sb thin films has been achieved by means of reactive magnetron co-sputtering under Ar/N_2 atmosphere. Film thicknesses, compositions and deposition homogeneity over the 200 mm substrate were controlled by means of X-Ray Reflectivity and Wavelength Dispersive X-Ray Fluorescence (WDXRF). The thicknesses of the films was fixed to 50 nm for Infrared and Raman spectroscopy and 200 nm for XAS/EXAFS measurements. After deposition, all OTS thin film samples were capped *in situ* by a 20 nm thick SiN layer without breaking of the vacuum in order to prevent surface oxidation.

For OTS selector devices fabrication, an OTS layer of a few tens of nm was deposited on a top of a 350 nm diameter W plug used as bottom electrode contact. Then, immediately after deposition of the OTS layer, a TiN top electrode was deposited without breaking the vacuum, preventing oxidation of the OTS layer. Leakage currents were measured at $V_{th}/2$ in quasi-static DC mode. Data were collected on 54 devices spatially distributed on the 200 mm substrate. The leakage current values correspond to

the median of the distribution, and the dispersion bars represent the values at more or less 34% around the median.

Raman spectra were acquired using a 532 nm laser on a µ-Raman spectrometer. Intensity and exposure time were optimized in order to avoid any modification of the material under the focused laser beam.

Fourier Transform Infrared spectroscopy analysis were performed in transmission mode. A sample consisting of only the 20 nm capping layer deposited on a Si substrate was used as reference sample for subtraction of the contributions of Si substrate and SiN layer to the FTIR spectra of OTS thin film samples.

To plot data of **Figure 4**, Sb-Sb, Se-Se and Ge-N modes were integrated after deconvolution of the different contributions of Raman spectra for Sb-Sb and Se-Se modes; and by integrating all the Ge-N absorption band of the FTIR spectra.

XAS measurements were carried out at the LISA beamline[42] using a Double Crystal fixed exit monochromator equipped with Si(111) crystals. In the different campaigns of data collection harmonic rejection was achieved either by Si-coated (E_{cutoff} = 15 keV with incidence angle of 2 mrad) or Pd-cated (E_{cutoff} = 18 keV with incidence angle of 3.6 mrad) mirrors for Se-K and Ge-K edges whereas for Sb-K edge Pt-coated mirrors (E_{cutoff} = 40 keV with incidence angle of 2 mrad) were used. Data were collected at T=300K in grazing incidence (incidence angle of 0.5 deg)[43] and the signal was collected in fluorescence mode using a 12 element High Purity Germanium detector. Two to four spectra per sample were collected in order to improve the signal-to-noise ratio.

XAS data were reduced with the ATHENA[44] code and modeled with the ARTEMIS[45] code. Theoretical EXAFS signals were calculated with the FEFF8.1[46] code starting from GaN, InN, GaAs, GaSb structures and the amplitude factors S_0^2 calibrated on experimental data. This choice was dictated from the fact that only for Ga and In well regular structures are available (wurtzite or zinc blende) and no major effect is expected passing from Ga to Ge or Se and from In to Sb because the central atom

and backscattering phase and amplitude functions are practically coinciding due to the similar atomic number. Data at the various K edges of the same sample were fitted simultaneously in order to minimize the number of free parameters.

Acknowledgements

This work has been partially supported by the European 621217 PANACHE and 783176 WAKeMeUP Projects. XAS measurements with synchrotron radiation were performed at the BM08/LISA beamline of the European synchrotron (ESRF) thanks to beamtimes under experience numbers 08-01-1037/MA-3993/MA-3995. Dr J.-B. Jager and Mr E. Delamadeleine from CEA-IRIG are also sincerely acknowledged for their invaluable support for XAS experiments. LISA is a project funded by the Consiglio Nazionale delle Richerche (project DFM.AD006.072).

Author contributions

P.N. and A.V. conceptualized the study and experiments. M.B. prepared the thin film samples in LETI clean rooms. G.N. supervised the OTS device fabrication in LETI 200 mm technological platform with help of M.B. A.V. performed and analysed all the electrical characterization of OTS devices with support of G.N. A.V. performed all Raman and FTIR spectroscopy experiments with support from J.-B.D. and P.N. XAS measurements were conceived by F.d'A. and realized by A.V., J.-B. D., P.N. and F. d'A. The XAS data were analysed by F.d'A. with advices from A.V. and P.N. The paper was written by A.V. and P.N. with help of F.d'A and G.N. All authors have given their approval to the final version of the manuscript.

References

[1] P. Noé, C. Vallée, F. Hippert, F. Fillot, J.-Y. Raty, *Semicond. Sci. Technol.* **2018**, *33*, 013002.

[2] T. Kim, H. Choi, M. Kim, J. Yi, D. Kim, S. Cho, H. Lee, C. Hwang, E.-R. Hwang, J. Song, S. Chae, Y. Chun, J.-K. Kim, in *2018 IEEE Int. Electron Devices Meet. IEDM*, IEEE, San Francisco, CA, **2018**, p. 37.1.1-37.1.4.

[3] G. Navarro, A. Verdy, N. Castellani, G. Bourgeois, V. Sousa, G. Molas, M. Bernard, C. Sabbione, P. Noe, J. Garrione, L. Fellouh, L. Perniola, in *2017 Symp. VLSI Technol.*, IEEE, Kyoto, Japan, **2017**, pp. T94–T95.

[4] M. Alayan, E. Vianello, G. Navarro, C. Carabasse, S. L. Barbera, A. Verdy, N. Castellani, A. Levisse, G. Molas, L. Grenouillet, T. Magis, F. Aussenac, M. Bernard, B. DeSalvo, J. M. Portal, E. Nowak, in *2017 IEEE Int. Electron Devices Meet. IEDM*, IEEE, San Francisco, CA, USA, **2017**, p. 2.3.1-2.3.4.

[5] D. Alfaro Robayo, G. Sassine, L. Grenouillet, C. Carabasse, T. Martin, N. Castellani, A. Verdy, G. Navarro, L. Ciampolini, B. Giraud, T. Magis, V. Beugin, E. Vianello, G. Ghibaudo, G. Molas,

E. Nowak, in *2019 IEEE Int. Mem. Workshop IMW*, IEEE, Monterey, CA, USA, **13/05**, pp. 132–135.

[6] H. Y. Cheng, W. C. Chien, I. T. Kuo, C. W. Yeh, L. Gignac, W. Kim, E. K. Lai, Y. F. Lin, R. L. Bruce, C. Lavoie, C. W. Cheng, A. Ray, F. M. Lee, F. Carta, C. H. Yang, M. H. Lee, H. Y. Ho, M. BrightSky, H. L. Lung, in *2018 IEEE Int. Electron Devices Meet. IEDM*, IEEE, San Francisco, CA, **2018**, p. 37.3.1-37.3.4.

[7] H. Y. Cheng, W. C. Chien, I. T. Kuo, E. K. Lai, Y. Zhu, J. L. Jordan-Sweet, A. Ray, F. Carta, F. M. Lee, P. H. Tseng, M. H. Lee, Y. Y. Lin, W. Kim, R. Bruce, C. W. Yeh, C. H. Yang, M. BrightSky, H. L. Lung, in *2017 IEEE Int. Electron Devices Meet. IEDM*, IEEE, San Francisco, CA, USA, **2017**, p. 2.2.1-2.2.4.

[8] J. Yoo, Y. Koo, S. A. Chekol, J. Park, J. Song, H. Hwang, in *2018 IEEE Symp. VLSI Technol.*, IEEE, Honolulu, HI, **2018**, pp. 207–208.

[9] N. S. Avasarala, G. L. Donadio, T. Witters, K. Opsomer, B. Govoreanu, A. Fantini, S. Clima, H. Oh, S. Kundu, W. Devulder, M. H. van der Veen, J. Van Houdt, M. Heyns, L. Goux, G. S. Kar, in *2018 IEEE Symp. VLSI Technol.*, IEEE, Honolulu, HI, **2018**, pp. 209–210.

[10] B. Govoreanu, G. L. Donadio, K. Opsomer, W. Devulder, V. V. Afanas'ev, T. Witters, S. Clima, N. S. Avasarala, A. Redolfi, S. Kundu, O. Richard, D. Tsvetanova, G. Pourtois, C. Detavemier, L. Goux, G. S. Kar, in *2017 Symp. VLSI Technol.*, IEEE, Kyoto, Japan, **2017**, pp. T92–T93.

[11] S. R. Ovshinsky, *Phys. Rev. Lett.* **1968**, *21*, 1450.

[12] A. Verdy, M. Bernard, J. Garrione, G. Bourgeois, M. C. Cyrille, E. Nolot, N. Castellani, P. Noe, C. Socquet-Clerc, T. Magis, G. Sassine, G. Molas, G. Navarro, E. Nowak, in *2018 IEEE Int. Electron Devices Meet. IEDM*, IEEE, San Francisco, CA, **2018**, p. 37.4.1-37.4.4.

[13] S.-Y. Shin, J. M. Choi, J. Seo, H.-W. Ahn, Y. G. Choi, B. Cheong, S. Lee, *Sci. Rep.* **2015**, *4*, 7099.

[14] A. Verdy, G. Navarro, V. Sousa, P. Noe, M. Bernard, F. Fillot, G. Bourgeois, J. Garrione, L. Perniola, in *2017 IEEE Int. Mem. Workshop IMW*, IEEE, Monterey, CA, USA, **2017**, pp. 1–4.

[15] P. Lucas, E. A. King, O. Gulbiten, J. L. Yarger, E. Soignard, B. Bureau, *Phys. Rev. B* **2009**, *80*, 214114.

[16] Z. G. Ivanova, E. Cernoskova, V. S. Vassilev, S. V. Boycheva, *Mater. Lett.* **2003**, *57*, 1025.

[17] P. Tronc, M. Bensoussan, A. Brenac, C. Sebenne, *Phys. Rev. B* **1973**, *8*, 5947.

[18] K. Jackson, A. Briley, S. Grossman, D. V. Porezag, M. R. Pederson, *Phys. Rev. B* **1999**, *60*, R14985.

[19] E. Baudet, C. Cardinaud, A. Girard, E. Rinnert, K. Michel, B. Bureau, V. Nazabal, *J. Non-Cryst. Solids* **2016**, *444*, 64.

[20] I. Chambouleyron, A. R. Zanatta, *J. Appl. Phys.* **1998**, *84*, 1.

[21] F. . Marques, I. Chambouleyron, F. Evangelisti, *J. Non-Cryst. Solids* **1989**, *114*, 561.

[22] G. Maggioni, S. Carturan, L. Fiorese, N. Pinto, F. Caproli, D. R. Napoli, M. Giarola, G. Mariotto, *Appl. Surf. Sci.* **2017**, *393*, 119.

[23] J.-Y. Raty, P. Noé, G. Ghezzi, S. Maîtrejean, C. Bichara, F. Hippert, *Phys. Rev. B* **2013**, *88*, 014203.

[24] J. Raty, *Phys. Status Solidi RRL – Rapid Res. Lett.* **2019**, *13*, 1800590.

[25] K. B. Borisenko, Y. Chen, S. A. Song, D. J. H. Cockayne, *Chem. Mater.* **2009**, *21*, 5244.

[26] I. Pethes, R. Chahal, V. Nazabal, C. Prestipino, A. Trapananti, S. Michalik, P. Jóvári, *J. Phys. Chem. B* **2016**, *120*, 9204.

[27] N. F. Mott, *Rev. Phys. Appliquée* **1977**, *12*, 619.

[28] A. Dahshan, K. A. Aly, *Philos. Mag.* **2008**, *88*, 361.

[29] J. S. Lannin, *Phys. Rev. B* **1977**, *15*, 3863.

[30] M. Ropo, J. Akola, R. O. Jones, *Phys. Rev. B* **2017**, *96*, 184102.

[31] K. S. Andrikopoulos, S. N. Yannopoulos, A. V. Kolobov, P. Fons, J. Tominaga, *J. Phys. Chem. Solids* **2007**, *68*, 1074.

[32] J. Y. Raty, W. Zhang, J. Luckas, C. Chen, R. Mazzarello, C. Bichara, M. Wuttig, *Nat. Commun.* **2015**, *6*, 7467.

[33] P. Noé, C. Sabbione, N. Castellani, G. Veux, G. Navarro, V. Sousa, F. Hippert, F. d'Acapito, *J. Phys. Appl. Phys.* **2016**, *49*, 035305.

[34] J. Luckas, D. Krebs, S. Grothe, J. Klomfaß, R. Carius, C. Longeaud, M. Wuttig, *J. Mater. Res.* **2013**, *28*, 1139.

[35] F. Zipoli, D. Krebs, A. Curioni, *Phys. Rev. B* **2016**, *93*, 115201.

[36] D. Ielmini, *Phys. Rev. B* **2008**, *78*, 035308.

[37] N. S. Avasarala, B. Govoreanu, K. Opsomer, W. Devulder, S. Clima, C. Detavernier, M. van der Veen, J. Van Houdt, M. Henys, L. Goux, G. S. Kar, in *2017 47th Eur. Solid-State Device Res. Conf. ESSDERC*, IEEE, Leuven, Belgium, **2017**, pp. 168–171.

[38] A. Verdy, G. Navarro, M. Bernard, P. Noe, G. Bourgeois, J. Garrione, M.-C. Cyrille, V. Sousa, E. Nowak, in *2018 IEEE Int. Mem. Workshop IMW*, IEEE, Kyoto, **2018**, pp. 1–4.

[39] R. W. Haisty, H. Krebs, *J. Non-Cryst. Solids* **1969**, *1*, 399.

[40] A. K. Bhatnagar, K. V. Reddy, V. Srivastava, *J. Phys. Appl. Phys.* **1985**, *18*, L149.

[41] C. H. Champness, R. H. Hoffmann, *J. Non-Cryst. Solids* **1970**, *4*, 138.

[42] F. d'Acapito, G. O. Lepore, A. Puri, A. Laloni, F. La Manna, E. Dettona, A. De Luisa, A. Martin, *J. Synchrotron Radiat.* **2019**, *26*, 551.

[43] C. Maurizio, M. Rovezzi, F. Bardelli, H. G. Pais, F. D'Acapito, *Rev. Sci. Instrum.* **2009**, *80*, 063904.

[44] M. Newville, *J. Synchrotron Radiat.* **2001**, *8*, 322.

[45] B. Ravel, M. Newville, *J. Synchrotron Radiat.* **2005**, *12*, 537.

[46] A. L. Ankudinov, B. Ravel, J. J. Rehr, S. D. Conradson, *Phys. Rev. B* **1998**, *58*, 7565.

Figure

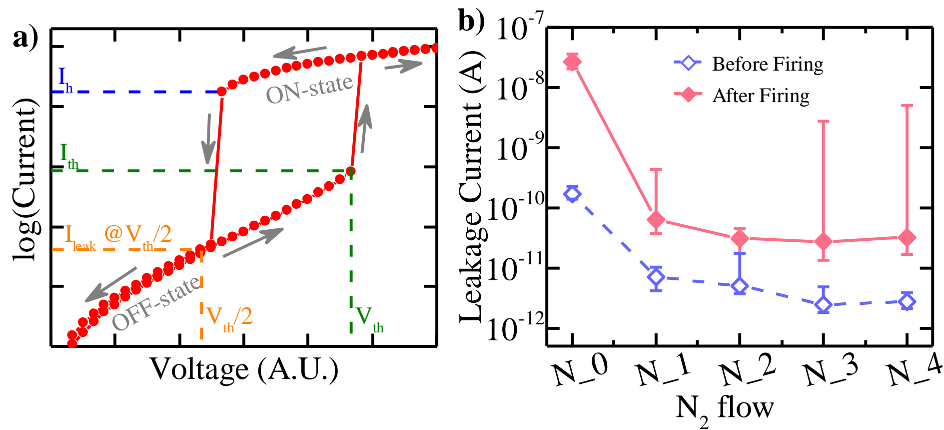

Figure 1. a) I-V characteristic of an OTS device describing the switching from the low-field highly resistive OFF-state to the highly conductive ON-state when the applied voltage exceeds the threshold voltage/current value (V_{th}/I_{th}). After the switching, when the applied voltage is decreased below V_{th}, the ON-state can be maintained down to the holding current (I_h), at which the material recovers its highly conductive OFF-state. The leakage current I_{leak} is defined as the current value measured at a voltage equal to $V_{th}/2$.

b) Evolution of the leakage current values and their dispersion from the median value measured on OTS devices (see **Experimental Section**) for different N contents labeled as N_x, being x representative of the N_2 flow used in Ar/N_2 plasma of the reactive sputtering deposition process of the OTS thin films. The introduction of N in $Ge_{24}Se_{56}Sb_{20}$ (GSS-N_0) films allows decreasing the leakage current. Furthermore, using an appropriate N content permits to obtain OTS devices exhibiting very low dispersion of the leakage currents, whereas high N contents are characterized by a broad dispersion towards high leakage current (see text).

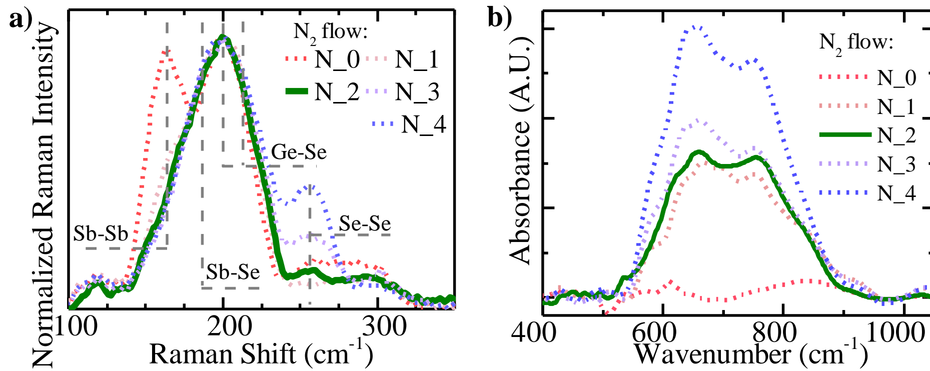

Figure 2. a) Raman spectra of N-doped Ge-Se-Sb films for different N contents labeled as N_x, being x representative of the N_2 flow used in Ar/N_2 plasma of the reactive sputtering deposition process. The main modes are reported in the figure. The main contributions correspond to Ge-Se and Sb-Se modes in $GeSe_{4/2}$ tetrahedrons and $SbSe_{3/2}$ pyramids, respectively. Compositions with a low N content exhibit Raman signature of Sb-Sb homopolar bonds, whereas for a high N content Se-Se bonds appear. For a specific N concentration (N_2), no homopolar Sb-Sb nor Se-Se bonds are observed in the Raman spectra.

b) Fourier-Transform Infrared (FTIR) spectroscopy acquired on the Ge-Se-Sb-N OTS thin films. The FTIR spectra are centered on the region of Ge-N absorption bands. After N introduction in the Ge-Se-Sb films, Ge-N bonds are formed with absorption modes centered around 700 cm^{-1}. The non-zero absorbance visible on the N-free Ge-Se-Sb film is a residual signal resulting from imperfect subtraction of contributions of the Si substrate and the 20 nm-thick SiN capping layer (see the **Experimental Section**).

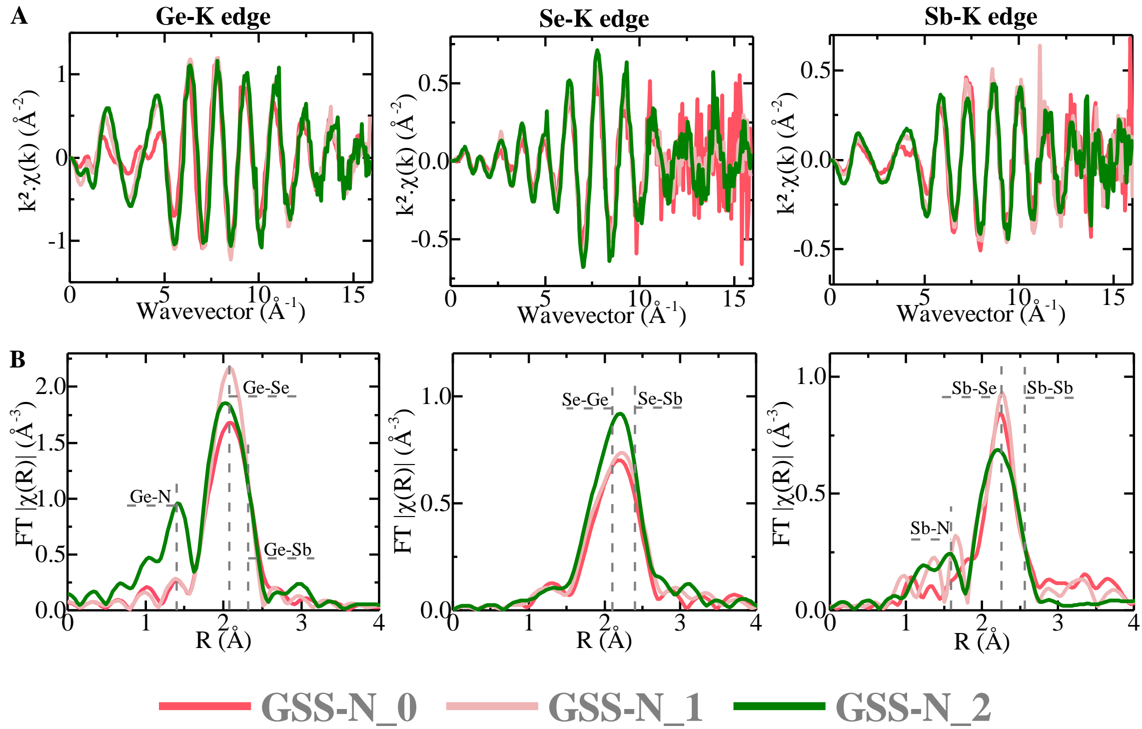

Figure 3. (**A**) Room temperature k^2-weighted EXAFS spectra and (**B**) their Fourier-transform acquired at Ge, Se and Sb K-edges on N-doped $Ge_{24}Se_{56}Sb_{20}$ thin films: GSS-N_0, GSS-N_1 and GSS-N_2 labels denote undoped and N-doped $Ge_{24}Se_{56}Sb_{20}$ films. The position of interatomic distances in the FT for the Ge-Se (Se-Ge), Sb-Se (Se-Sb), Ge-N and Sb-N bonds are indicated by vertical dashed lines.

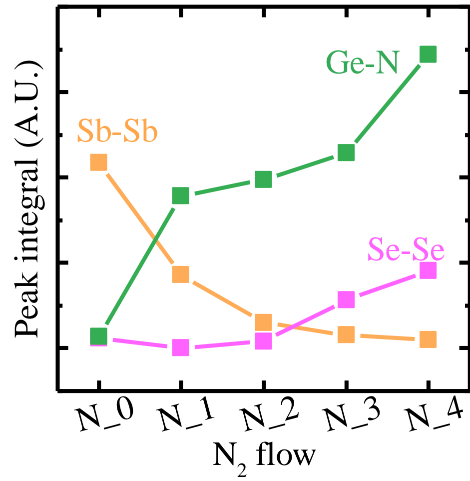

Figure 4. Change of the number of Sb-Sb, Se-Se and Ge-N bonds as a function of the N_2 flow used for the reactive deposition of the $Ge_{24}Se_{56}Sb_{20}$ films. The plotted values were obtained by integration of the contribution of the modes in Raman and FITR spectra (see the **Experimental Section**). For the optimized GSS-N_2 sample, the number of both Sb-Sb and Se-Se homopolar bonds is close to zero.

The critical role of homopolar and wrong bonds in amorphous Ge-Se-Sb-N films on the performance of OTS selector devices is here investigated. Using a proper concentration of N during reactive sputtering deposition of the films, is shown to be a key engineering tool of the amorphous structure allowing to remove such detrimental bonds and thus achieving reliable OTS materials.

Keyword Ovonic effect

Anthonin Verdy, Francesco d'Acapito, Jean-Baptiste Dory, Gabriele Navarro, Mathieu Bernard, and Pierre Noé**

Effect of nitrogen on the amorphous structure and subthreshold electrical conduction of GeSeSb-based OTS thin films

ToC figure ((Please choose one size: 55 mm broad × 50 mm high **or** 110 mm broad × 20 mm high. Please do not use any other dimensions))

Supporting Information

Effect of nitrogen on the amorphous structure and subthreshold electrical conduction of GeSeSb-based OTS thin films

Anthonin Verdy, Francesco d'Acapito, Jean-Baptiste Dory, Gabriele Navarro*, Mathieu Bernard, and Pierre Noé**

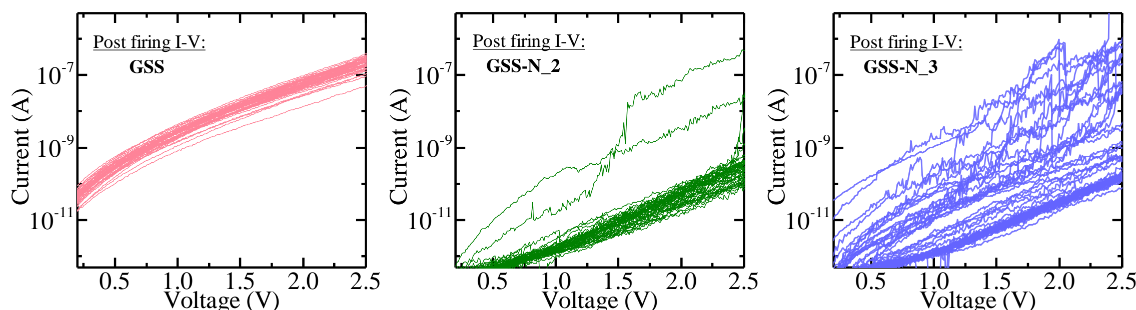

Figure S1. I-V characteristics of GSS, GSS-N_2 and GSS-N_3 samples measured after firing step. GSS samples are characterized by high leakage currents. Despite few devices showing high leakage current, GSS-N_2 devices exhibit a low dispersion of the leakage current values. On the contrary, GSS-N_3 devices feature a huge device-to-device dispersion of the sub-threshold characteristics, added to an important noise.

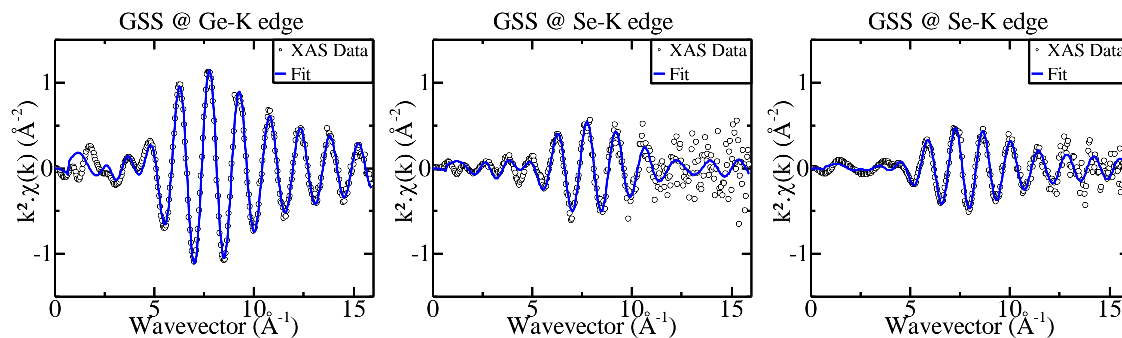

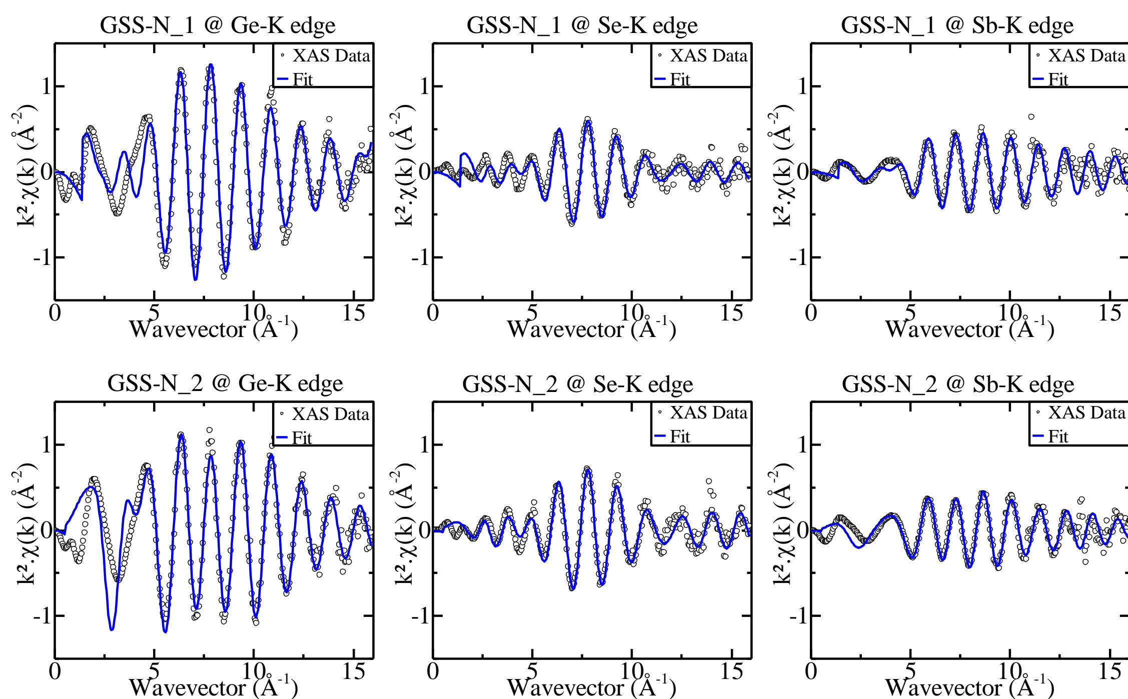

Figure S2. Plots of the experimental k^2-weighted EXAFS data (dots) and fitting curves (lines) acquired at Ge, Se and Sb K-edges for the GSS, GSS-N_1 and GSS-N_2 samples (see main text).

Ge-K edge	**Ge-Se**			**Ge-Sb**			**Ge-N**		
	N	R (Å)	σ^2 (Å^2)	N	R (Å)	σ^2 (Å^2)	N	R (Å)	σ^2 (Å^2)
GSS	2.3(1)	2.39(1)	0.0033(1)	0.7(1)	2.64(1)	0.005(1)	-	-	-
GSS-N_1	2.7(3)	2.40(2)	0.005(3)	-	-	-	1.3(3)	1.84(2)	0.004(2)
GSS-N_2	2.3(4)	2.37(1)	0.0034(7)	-	-	-	2(1)	1.84(2)	0.005(4)
Se-K edge	**Se-(Se/Ge)**			**Se-Sb**			**Se-N**		
	N	R (Å)	σ^2 (Å^2)	N	R (Å)	σ^2 (Å^2)	N	R (Å)	σ^2 (Å^2)

GSS	1.2(1)	2.39(1)	0.0033(1)	0.6(1)	2.63(2)	0.004	-	-	-
GSS-N_1	1.2(2)	2.38(2)	0.005(3)	0.8(1)	2.65(4)	0.004	-	-	-
GSS-N_2	1.5(2)	2.37(1)	0.0034(7)	0.8(1)	2.63(2)	0.004	-	-	-
Sb-K edge	**Sb-Sb**			**Sb-(Se/Ge)**			**Sb-N**		
	N	R (Å)	σ^2 (Å^2)	N	R (Å)	σ^2 (Å^2)	N	R (Å)	σ^2 (Å^2)
GSS	0.8(3)	2.87(2)	0.004(2)	3.1(1)	2.63(2)	0.004	-	-	-
GSS-N_1	-	-	-	3.5(2)	2.65(2)	0.004	2(2)	2.00(2)	0.01(1)
GSS-N_2	-	-	-	3.4(2)	2.63(2)	0.004	2(2)	2.00(2)	0.010(7)

Table S3. Quantitative results of the EXAFS data analysis. N, R and σ^2 correspond respectively to the coordination number, the interatomic distance and the Debye-Waller factor. In principle, it is not possible to distinguish X-Ge from X-Se bonds for any X central atom due to the similarity of backscattering functions of Ge and Se. However, the Ge-Se bond has here been interpreted as heteropolar because the homopolar bond would have a longer distance (4 coordinated Ge is at 2.45 Å). The others like Se-(Ge/Se) and Sb-(Ge/Se)) cannot be safely distinguished and additional can be derived from RAMAN spectroscopy.